Research Article Vol. 6, No. 5 / May 2019 / Optica 608

In vivo volumetric imaging by crosstalk-free full-field OCT

Patrycjusz Stremplewski, Egidijus Auksorius, Paweł Wnuk, Łukasz Kozoń, Piotr Garstecki, and Maciej Wojtkowski*

Institute of Physical Chemistry, Polish Academy of Sciences, Kasprzaka 44/52, 01-224 Warsaw, Poland
**Corresponding author: mwojtkowski@ichf.edu.pl*

Received 25 February 2019; revised 8 April 2019; accepted 8 April 2019 (Doc. ID 360929); published 7 May 2019

Cellular resolution imaging of biological structures has always been a challenge due to strong scattering that limits the achievable transverse resolution or imaging penetration depth. Recently, a major advancement toward high-resolution and volumetric imaging was achieved by implementing a parallel detection (i.e., full field) into Fourier-domain optical coherence tomography. The drawback of using parallel detection is that scattered light can travel laterally and get mapped improperly at a camera creating optical crosstalk, which severely impairs the interpretation of subcellular images and limits its use in medical diagnostics. In this work, we demonstrate for what we believe is the first time how to efficiently reduce crosstalk and enable microscopic quality volumetric reconstructions of the scattering tissue-like human skin *in vivo*, all within less than a half of a second. To minimize crosstalk, we implemented a very fast deformable membrane that introduces random phase illumination. Additionally, the sample is illuminated under variable angles to reduce the contrast of speckles by incoherent summation of the crosstalk-free volumes. Introducing crosstalk and speckle-free OCT will advance imaging prospects closer to the ideal of a noninvasive optical biopsy.

https://doi.org/10.1364/OPTICA.6.000608

1. INTRODUCTION

The remarkable development of optical imaging methods that has taken place in recent decades brings us closer to noninvasive microscopic imaging of cells embedded in the tissues of living organisms. Special attention should be paid to optical methods providing information about the amplitude and phase, which can be further processed by advanced computational techniques to create volumetric reconstructions. One such modality is optical coherence tomography (OCT), which is a family of imaging technologies based on low-coherence interferometry [1,2].

There are currently more than a dozen different ways to exploit low-coherence imaging in competitive scenarios, including time versus Fourier domain detection, full-field versus scanning (confocal) configurations, *en face* versus B-scan acquisition, and swept-source versus spectrometer-based detection [2–5]. To obtain an appropriate signal-to-noise ratio (SNR) of optical reconstructions, most of the OCT techniques use spatially coherent light with adequately high optical density values.

Unfortunately, spatially coherent radiation severely impairs the interpretation of cross-sectional images and limits its use in medical diagnostics by the presence of speckles in OCT reconstructions [6–10]. Recently, we demonstrated that it is possible to emulate the spatial incoherence by using spatio-temporal optical coherence manipulation (STOC), which tailors the effective fringe visibility of spatially coherent radiation [11,12]. This method can only be effectively applied to full-field OCT (FF-OCT) since it requires spatial mode mixing for different locations in space, which is impossible in scanning OCT systems. It is especially advantageous to apply such solutions to Fourier-domain full-field OCT (Fd-FF-OCT), which benefits from higher speed and improved SNR [13–16].

In the scanning OCT devices, the signal-degrading contributions from multiply scattered light are reduced by an aperture placed before the detector, which is usually implemented in the form of a single-mode fiber [7,9,17,18]. This approach is like the designs in classical confocal microscopy. Therefore, in the most typical OCT applications, the contribution of the signal-degrading speckle pattern is less pronounced, and the dominating source of coherence noise becomes signal-carrying speckle patterns [18]. The remaining part of multiply scattered light, which is not filtered by the confocal gating, contributes to the coherence signal only in the in-depth direction causing axial delocalization of the OCT signal by forming artificial "tails" in optical A scans [19]. Additionally, the sensitivity of OCT is greatly improved by a rejection of most of the multiply scattered waves that additionally experience optical delays longer than the coherence time (temporal coherence gating). The combination of those two filtering mechanisms is critical to achieve high-quality reconstructions of living tissue.

Full-field OCT methods do not use transversal scanning of the focused probing beam. Instead, the interferometric signal is recorded in parallel for all transverse points of the illuminated sample by a matrix of photodetectors, such as in CMOS or CCD cameras. Single-scattered or reflected light waves coming from

separate sample points belonging to the same *en face* plane do not interfere with each other at the camera because of their spatial separation in the imaging plane. However, if light gets scattered multiple times in a sample, it could travel laterally and get mapped improperly at a camera. Similar to other OCT methods, the interference occurs if the optical path difference between waves backscattered from an object and reflected from the reference mirror is close to the coherence length of the light source. Light waves improperly mapped on a camera also will be randomly delayed. Therefore, they will significantly contribute to the AC component of the FF-OCT signal, creating the so-called optical crosstalk-generated noise (crosstalk) [17,18]. The crosstalk can be rejected using a spatially low coherent light source, but the price is paid in *s* very limited axial imaging depth caused by a fast decorrelation between the reference and the object signals with introduced defocus [20–24]. Such spatial coherence gating (SCG) [25–27] can be controlled by additional spatial filtering of incoherent radiation. However, such procedures will further compromise the power density and create limitations to applying such methods *in vivo*.

In this work we demonstrate that high-speed dynamic random phase modulation of spatially coherent radiation implemented in Fourier domain full-field OCT reduces crosstalk-generated noise. Using a high-speed deformable membrane (DM) as a phase modulator introduces partial spatial coherence with controlled SCG. That action in turn permits a FD-FF-OCT method free of crosstalk with an axial imaging depth in the range of millimeters, thus enabling real-time *in vivo* imaging.

2. OPERATION PRINCIPLE

Our method filters unwanted crosstalk by applying a mechanism analogous to confocal gating but is based purely on the interferometric effect of fringe washout on multiply scattered light. Inspiration for the development of a crosstalk-free full-field OCT technique came from the method known as dynamic random phase illumination used in interferometric microscopy [24,25,28] and holographic quantitative phase microscopy (QPM) [23,29]. These techniques combine interferometric detection with the SCG to improve axial sectioning [24,28]. In these approaches, each spatial mode plays the role of a virtual pinhole, since interference only occurs for light from a single spatial mode [28,30]. For all these techniques, the random phase illumination is introduced by a rotating diffuser placed in front of the interferometer or spatially coherent laser arrays and a multimode fiber causing temporal and spatial modulation of coherent laser light. To minimize the depth of field (DOF), the illumination pupil plane of the objective lens is fully filled. In contrast to interferometric microscopy, in Fourier-domain OCT a much longer DOF is desired because it inherently defines the axial extent over which images can be acquired. The axial resolution is then defined by either the DOF or the coherence length of the light source, whichever is smaller.

The first attempt to apply the dynamic random phase illumination to FD-FF-OCT was demonstrated by Povazay *et al.* [16]. In that approach the crosstalk was reduced by mixing the high number of differently populated transversal modes in the multimode fiber by microbending at acoustic frequencies. Light from the multimode fiber illuminated a thick diffuser for more uniform distribution of the Gaussian intensity profile. Thus, the effective random phase illumination field was not uniquely mapped on an individual plane within the object. Unfortunately, the authors did not quantify the reduction of crosstalk. the study also was missing an analysis of the SCG effect introduced by the dynamic random phase illumination. Based on the results presented in the paper one can deduce that, similar to interferometric microscopy and QPM, the DOF was dramatically reduced, which prevented high-quality OCT imaging.

We control the SCG and the reduction of the crosstalk-generated noise by employing a DM [31] placed in front of the OCT interferometer (Fig. 1). In contrast to previously reported techniques, here a well-localized plane corresponding to the surface of the DM is conjugated to the sample and the reference mirror planes. Thus, the dynamic spatial phase modulation introduced across the wavefront by the DM is uniquely mapped on a well-defined plane within the object. Such localized spatial coherence reduction ensures that interferometric fringes will occur only for identically divergent beams coming from the sample and the reference arm of the interferometer (fringes of equal inclination, which are known as Haidinger fringes) [32]. These fringes will not wash out in the focus because both interferometer

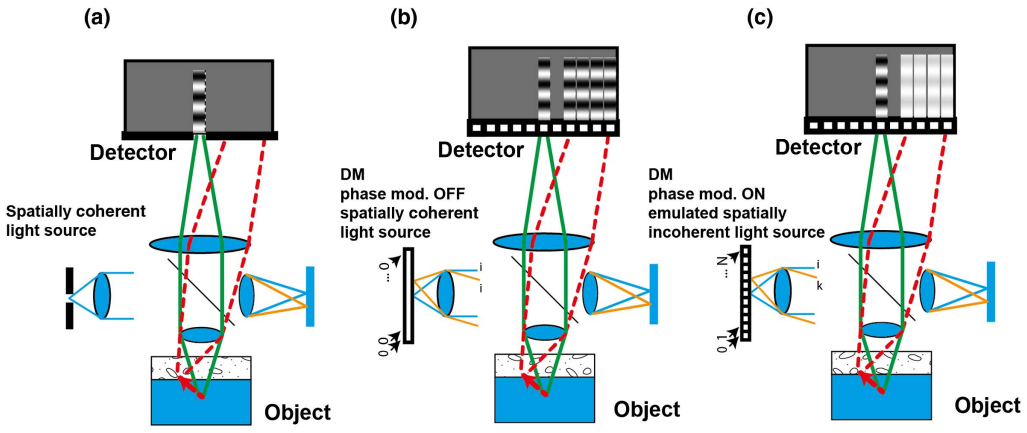

Fig. 1. Principle of crosstalk-free FD-FF-OCT: (a) Multiply scattered light can be rejected by using a pinhole placed in the front of the photodetector—the solution used in scanning OCT devices; (b) Origin of the crosstalk: Full-field OCT with spatially coherent illumination uses numerous detection channels, hence the multiply scattered light contributes to interference in pixels that are improperly mapped with respect to the real image of the measured object; (c) Crosstalk-free FF-OCT: The spatial phase modulation introduced by the deformable membrane (DM) placed in front of the interferometer washes out fringes originating from multiply scattered light, effectively reducing the crosstalk.

arms see identical speckle fields. This is the main mechanism behind the crosstalk removal since multiply scattered light in the object arm will lack the corresponding image in the reference arm. Therefore, multiply scattered light responsible for the crosstalk eventually does not contribute to the interference signal.

By introducing the control of SCG we introduce another degree of freedom to OCT imaging. As mentioned above, the introduction of dynamic random phase illumination leads to the additional axial sectioning by SCG. A three-dimensional (3D) speckle field created by the dynamic random phase modulation decorrelates quickly along the optical axis for each diffraction-limited spot on a sample if the pupil plane of the objective is filled. For single-scattered or back-reflected light the phase across the beam remains correlated uniquely for each transverse point only in the focal plane as it gets blurred and starts to crosstalk with neighboring pixels when moving away from the focus. The axial range over which the phase remains correlated is defined by the size of the spatial coherence area (SCA) [33], which in turn depends on the effective size of a single active element of the spatial phase modulator and the magnification factor of optical elements between the phase modulator and the sample. In the Linnik interferometer configuration and for SCA larger than the diffraction limited spot, the interferometric fringes will be visible even if light is significantly defocused in one of the interferometric arms. The fringe visibility will decrease with the increase of defocus until the blurred point spread function (PSF) reaches the size of the SCA. This effect gives a net result analogous to the confocal gating that is present in scanning OCT systems. Here the temporal coherence gating, provided by the coherence length of the light source and SCA, also both overlap to generate crisp OCT images.

The 3D speckle field generated within the DOF changes at the rate of DM operation frequency and is averaged out to a uniform distribution within the integration time of a single camera frame. Therefore, the phase modulation must be fast enough so that light at these points undergoes full de-correlation within the integration time of a camera frame. Subsequently, the crosstalk effect in FD-FF-OCT is reduced by ensuring that the light coming from neighboring locations adds up incoherently on a camera and forms a relatively uniform background. Cameras running at $>50,000$ frames per second are used in the best-performing FD-FF-OCT systems; therefore, to generate the uncorrelated phase/speckle dynamics, the phase modulation should be carried out approximately at a rate that is an order of magnitude faster, which would be around 500 kHz. This difficult task is accomplished here by using a customized DM. This instrument is placed in front of the interferometer so that the same phase pattern is imaged onto the sample and the reference mirror, which ensures that interferometric fringes corresponding to single backscattering will survive.

3. EXPERIMENTAL SETUP AND IMAGE PROCESSING

The basic scheme of our setup is presented in Fig. 2. A detailed description of the optical system is in Supplement 1. The system is composed of a Linnik interferometer with identical optical elements in the reference and object arms. Acquisition is performed with a fast camera (Fastcam SA-Z), which allows the collection of 12-bit images at a rate of up to 21 GS/s. The light source is a fast-tunable laser (Superlum Broadsweeper BS-840-2-HP) that can

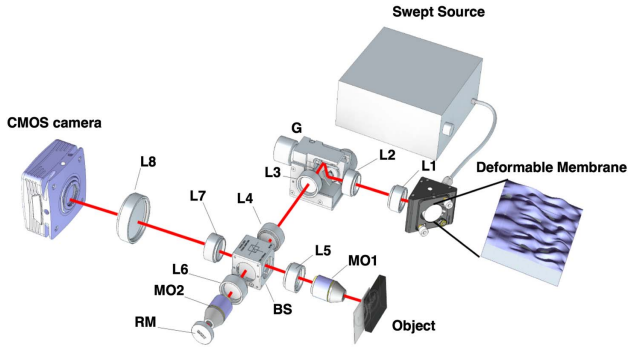

Fig. 2. Scheme of the FD-FF-OCT setup capable of crosstalk and speckle noise suppression: L1–L8, achromatic doublet lenses; G, galvo scanner introducing additional angular compounding; MO1 and MO2, 10 × Olympus objectives with 0.3NA; RM, reference mirror; BS, beam splitter.

deliver 20 mW average output power and is tuned from 800 to 878 nm at a sweeping speed of up to 100 000 nm/s.

A collimated beam of 4 mm in diameter hits the customized DM from Dyoptica, which performs up to 500,000 chaotic vibrations per second. Thus, it introduces uncorrelated phase modulation patterns across the beam at a rate far higher than the camera's inversed exposition time. The beam is modulated in such a manner that it is no longer spatially coherent. The plane corresponding to the surface of the DM is conjugated to the plane of the galvo-scanner GM, and to the planes of the reference mirror and the object. The measured transverse resolution value was found to be 2.5 μm (see Supplement 1), which is close to the theoretical diffraction limited resolution (calculated for the objective of NA = 0.3, the central wavelength of 840 nm and non-coherent radiation).

The optical power delivered to the sample is far below ANSI standards for safe illumination of living tissue since we use a Gaussian beam of 1 mm diameter at $1/e^2$ with 4.5 mW, which results in the optical power per one camera pixel at the level of 20 nW. The measured sensitivity of the FD-FF-OCT system with the DM switched on and corresponding to the above-mentioned optical power is 71 dB for the exposure time of 18 ms, which is the time required to collect a 512 × 512 × 1024 pixel volume of FD-FF-OCT data (512 × 512 × 512 pixels after FFT). The sensitivity dropoff is 2.5 dB at 1 mm and 15 dB at 2 mm. The measured axial resolution is 6 μm after spectral shaping with a Gaussian window ensuring 25 dB suppression of side lobes of the axial point spread function (PSF). The measured value of the dynamic range (DR) of the system is 58 dB. Both the sensitivity and the DR values are below the requirements for *in vivo* imaging due to limited power density generated by the wavelength-swept laser; therefore, we decided to perform multiple measurements to improve both parameters. We identified an optimal number of 36 volumes that enabled 93 dB sensitivity and 75 dB of DR within 0.7 s of the total measurement time (see Supplement 1).

To further optimize the performance of the imaging system and take advantage of an averaging process, we introduced angular compounding [34–37]. It was achieved by shifting the focused probing beam in the back focal plane of the objective, which enabled changing the direction of the beam impinging onto a

sample and the reference mirror. In practice it was realized by placing a pair of galvo scanners (GM) between the DM and the interferometer. For each measured volume we changed the illumination angle on the sample and the reference mirror to reduce the speckle noise in the resultant OCT reconstructions. This configuration ensures that the condition of identical spatial distribution of phase modulation is preserved for both the reference mirror and the sample. The efficiency of the speckle reduction was quite poor—reducing the speckle contrast by a factor of two in the focal plane and by a factor of 3.5 in the defocused region with six times poorer transverse resolution (~20 μm) (details are described in Supplement 1).

Proportions between the number of pixels in the X, Y, and Z directions can be varied by changing the camera settings and the sweep rate of the laser. In our experiments, we used two basic configurations. For tests on static phantoms, we acquired 1024 images with 512 × 512 pixels each at a rate of 60.000 fps while the laser was tuned from 800 to 878 nm in 17 ms (sweep rate of 4500 nm/s). To reduce the measurement time for *in vivo* experiments we cut the number of acquired images to 548, resulting in 9 ms total acquisition time (sweep rate of 8400 nm/s).

All images were stored in the camera's internal memory and, after the acquisition process finished, they were sent to the computer memory for processing. We performed 3D reconstruction in the same way as in any Fourier domain imaging—the time series acquired by each camera pixel is Fourier transformed to form A scans [38]. Acquired volumes are processed independently and the final 3D intensity data (modules of FT data points) are averaged. because the communication between the computer and the camera is done by Ethernet connection, the time to transfer data is reduced compared to systems equipped with a dedicated camera—computer interface, such as a camera link. Therefore, it was challenging to get a preview mode to enable a real-time object alignment procedure, like in typical scanning OCT devices. We overcame this problem by reducing the active area of the camera sensor to 128 × 8 pixels^2. A total of either 1024 or 548 images were then collected at a normal frame rate and sweep rate of the laser (equivalent to a standard FD-FF-OCT), and sent for processing and to obtain preview B scans roughly once per second. B scans comprising 128 A scans cover a quarter of the width of the imaging area, which is sufficient for a sample alignment procedure. When the object is at the right position, we switch to data collection mode and capture the desired number of frames covering the entire area of interest (512 × 512 pixels^2).

4. SPATIAL COHERENCE GATING INTRODUCED BY THE HIGH-SPEED DM

To test the effect of the SCG in isolation from the temporal coherence gating, a narrowband (<0.1 nm) laser illumination was used at the central wavelength of 840 nm. This ensured that the optical sectioning effect was not due to the temporal coherence gating but SCG only. The narrowband illumination was carried out by operating the laser source in a nonsweeping, fixed-wavelength mode. To measure the SCG effect, we used a mirror that was placed in the focal plane of the sample arm of the interferometer and the DM was effectively imaged onto both mirrors, as can be seen in Fig. 2. One of the mirrors was slightly tilted to produce interferometric fringes on the camera. The fringes in this configuration appeared regardless if the DM was active (randomizing the wavefront phase) or inactive, as shown in Fig. 3(a) (middle). The fringes disappeared if one of the mirrors was

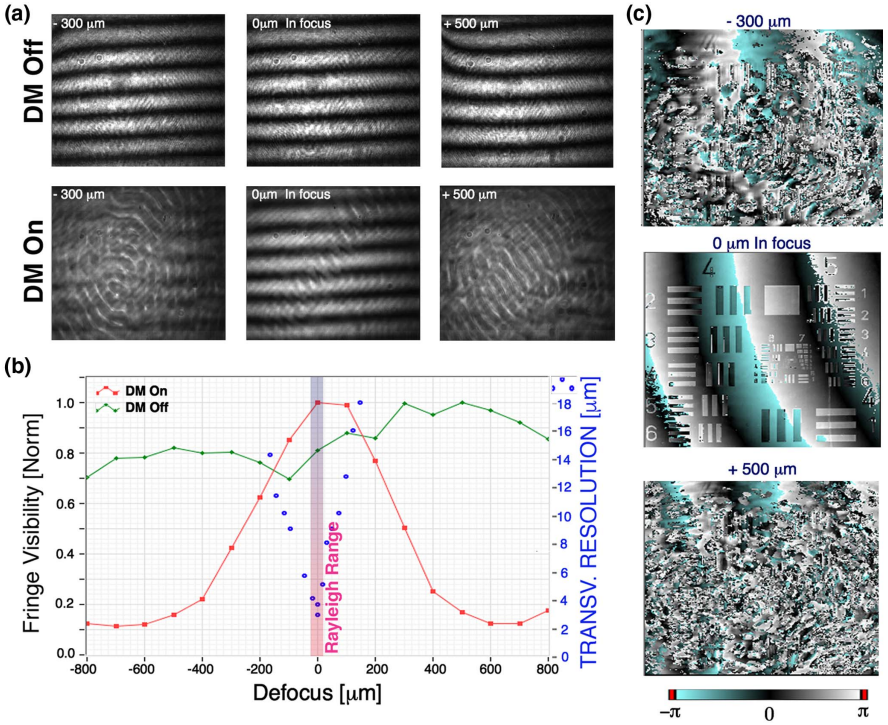

Fig. 3. (a) Interferometric fringe visibility as a function of defocus recorded at three defocus values (−300 μm, 0 μm, and 800 μm) with DM in inactive (top) and active (bottom) states. (b) Fringe visibility curves estimated as a function of defocus when DM is in the active (red) and inactive (green) states. Decrease of resolution as a function of defocus is shown for comparison purpose (blue dots). Pink bar corresponds to the theoretical value of the DOF. (c) Phase decorrelation as a function of defocus recorded at three defocus values (−300 μm, 0 μm, and 800 μm) with DM in active state.

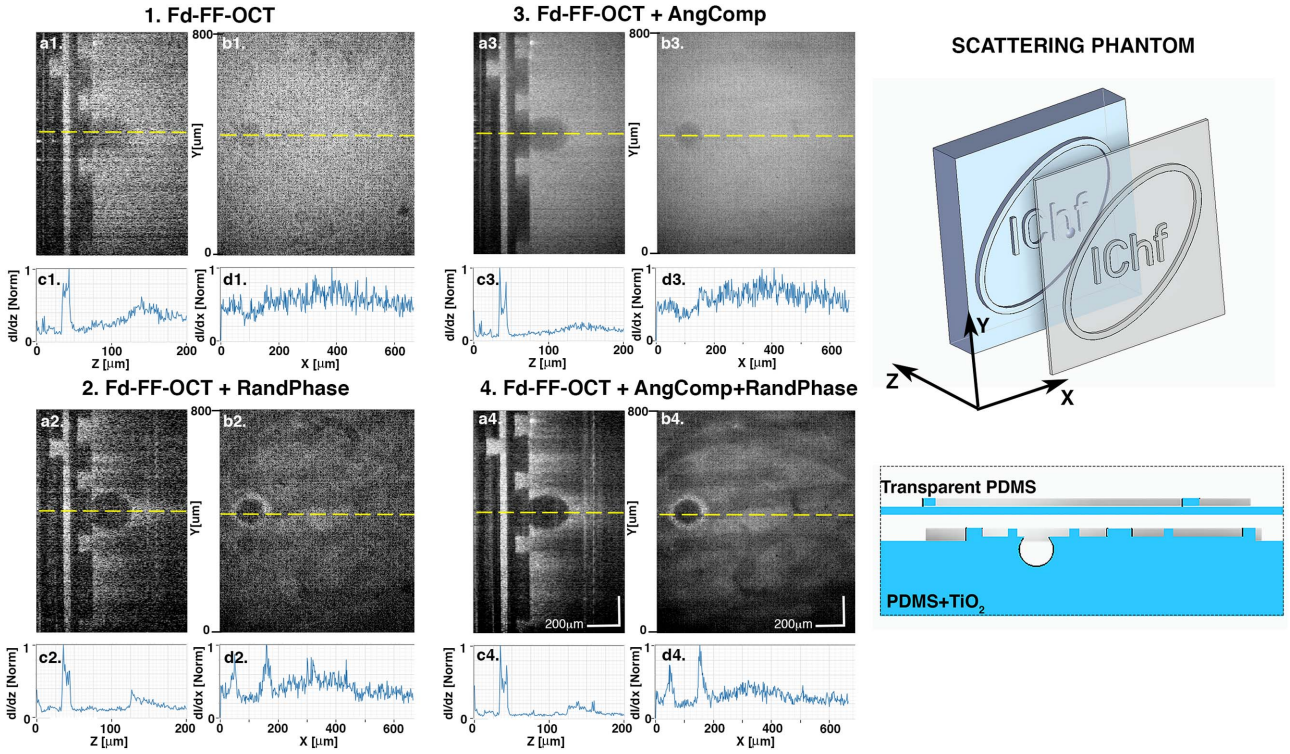

Fig. 4. Crosstalk and speckle removal using random phase illumination (RandPhase) and angular compounding (AngComp): (a) cross-sectional images parallel to the direction of light propagation -optical B-scans; (b) cross-sectional images in the plane transverse to the direction of light at a depth of 500 μm below the surface of the phantom; and (c), (d) derivative of the spatial distribution of the backscattered signal intensity calculated along the yellow dashed lines marked on images (a) and (b).

translated along the optical axis (defocused) when the DM was "on," as illustrated in Fig. 3(a) for 300 and 800 μm defocus from the focal plane. The fringes remained irrespective of the defocus when the DM was "off." This situation could be easily explained. When the DM is "off," the beam going toward the mirror is collimated and its wavefront is flat. The camera also sees the flat

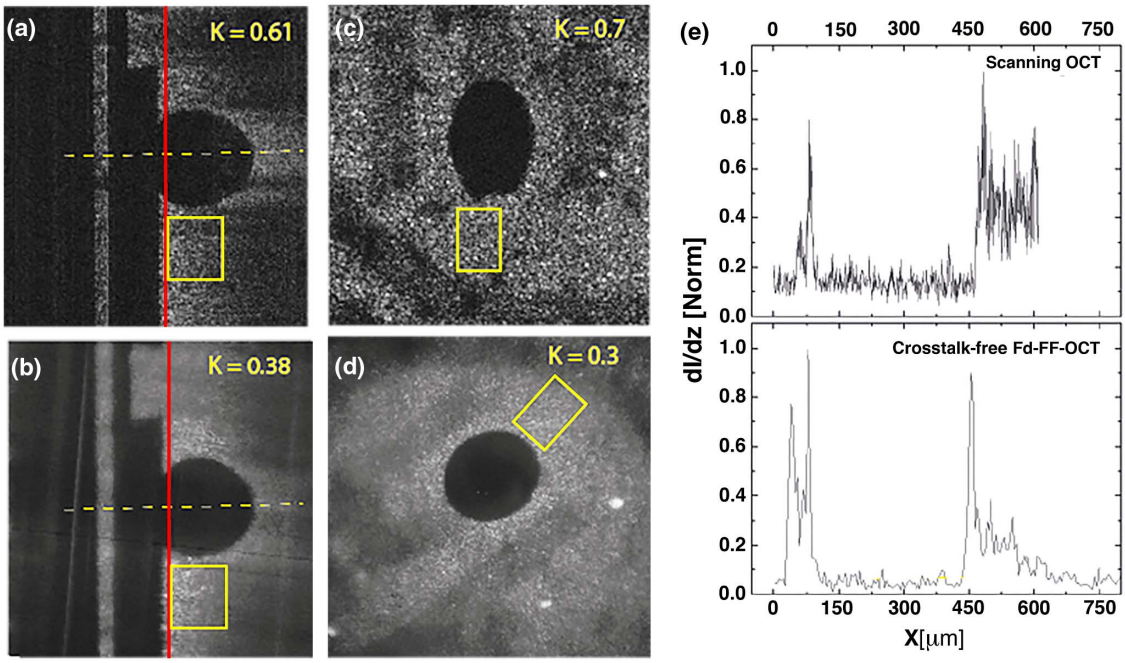

Fig. 5. Comparison of scanning OCT and crosstalk-free FD-FF-OCT systems performed on 3D scattering phantom: (a) cross-sectional image (optical B scans) measured by scanning OCT (YZ plane), (b) crosstalk-free FD-FF-OCT cross-sectional image; (c), (d) XY cross-sectional images corresponding to the axial planes indicated by red lines; and (e) LSFs calculated along yellow dashed lines marked in panels (a), (b). Yellow boxes indicate areas used to calculate the speckle contrast K.

wavefront, which does not change when the mirror is being defocused. This produces a stable fringe pattern that only shifts laterally with the axial mirror translation. However, when the DM is "on" the beam is no longer collimated but impinges the sample and the reference mirror at many different angles. This happens because the DM effectively acts as a phase grating diffracting beam at many different random angles. Since the beam will now have a wavefront that is not flat and evolves along the optical axis, moving the mirror out of focus will significantly decrease the contrast of the interference pattern. Figure 3(b) summarizes the effect of the DM in the "on" and "off" states by displaying fringe visibility curves, which effectively correspond to the optical sectioning curves.

To derive those curves, the mirror was translated along the optical axis and the fringe visibility was calculated by performing FFT along a single line perpendicular to the fringe pattern. Peak values of the amplitude spectrum were extracted and plotted in arbitrary units against the defocus, shown in Fig. 3(b). The estimated FWHM value of the optical sectioning curve was 565 μm at the FWHM of the Gaussian profile (1.1 mm at $1/e^2$), indicating the axial range over which SCG suppresses the crosstalk. To understand the extent of introduced defocus, Fig. 3(b) also shows the actual transversal resolution loss (in blue points). The estimated Rayleigh range or DOF = 56 μm at FWHM and ∼65 μm at $1/e^2$ is also indicated as a pink bar. In contrast to the scanning OCT device and a typical confocal system, the SCG in our case is decoupled from the numerical aperture of the objective lens and it is 17 times longer than the Rayleigh range, resulting in an SCA 17 times larger than the diffraction-limited PSF.

The surface of the deformable mirror is continuous and relatively smooth, so there are no rapid changes of phase and the illumination field incident on the sample is uniform in vicinity of the focal plane [see the central picture in the upper row of Fig. 3(a)]. The phase modulation introduced by the DM results in a stationary intensity pattern away from the focal plane [see Fig. 3(a), −300 μm and +500 μm away from focal plane when the DM is On]. Figure 3(c) shows the variation of the spatial distribution of the stationary phase with an introduced defocus. The spatial distribution of the phase randomizes with an increased defocus with the average size of the phase-modulating element being tens of micrometers.

5. IMAGING OF 3D SCATTERING PHANTOM

Figure 4 shows an example of 3D imaging of a phantom composed of transparent PDMS material with two scattering layers made from a mixture of PDMS and TiO2 powder (more information about the fabrication process to obtain the phantom can be found in Supplement 1). On each side of the scattering layer, there are protruding "ICHF" logotypes, which are transversally offset from each other. One scattering layer with a thickness of about 30 μm (90 μm including the logotype) is around 50 μm above the second layer, the thickness of which is a few millimeters. These logotypes are made of the same scattering material. In the cross-sectional images of Figs. 4(a1)–4(a4), fragments of the logotypes have the shape of rectangular blocks "growing out" of the scattering layers. In addition, in the thicker layer of the diffuser there is a spherical cavity with a diameter of about 180 μm (air bubble trapped during the molding process). Figure 4 compares cross-sectional images obtained with the standard FD-FF-OCT apparatus [Fig. 4(1)] against images obtained with the setup reported here [Figs. 4(2)–4(4)].

Figure 4(a) show cross-sectional images in the plane parallel to the direction of light propagation (in the YZ plane), while the Fig. 4(b) show cross-sectional images in the plane transverse to the direction of light (XY) at a depth of 500 μm below the surface of the phantom. The reconstruction of the scattering base in the panels 4(a3) and 4(b3) looks homogenous because of the domination of the crosstalk. More realistic reconstructions are visible in panels 2 and 4. According to the Lambert–Beer law, light is attenuated when passing through the superficial layer. More attenuation is visible when light passes longer paths through ICHF scattering letters, causing "shadowing" and a projection of the ICHF logo onto the lower scattering layer. Also, the Lambert–Beer law is not obeyed in the reconstruction presented in the panel 4(c3), once panels 4(c2) and 4(c4) show an exponential attenuation of the registered signal with imaging depth.

To quantify the improvement of the imaging quality we decided to analyze the local contrast factor. It was calculated by taking the derivative of the intensity profile of the backscattered signal on the sample along lines cutting through boundaries between the nonscattering and scattering areas. Such a function applied to our data is similar to the line spread function (LSF), which reflects both contrast and resolution at once [39]. LSF allows visualization of the edges of objects. If the contrast is high and the edges are clearly visible, then the derivative signal should show the peak in a place corresponding to the location of the expected edge. In the case of the analyzed structure, it was assumed that the edges of the spherical cavity located in the scattering layer should be well visualized using such a derived signal. In the case of standard FD-FF-OCT, the edges of the cavity are not visible either in the YZ cross-section or in the XY cross-section [Figs. 4(a1) and 4(b1)]. This is confirmed by LSFs calculated along the lines marked on these cross-sectional images [Figs. 4(c1) and 4(d1)]. After applying the random phase modulation, the edges of the cavity become clearly visible in both projections [Figs. 4(c2) and 4(d2)]. Application of the spatial phase modulation made it possible to get rid of the crosstalk effects, thereby increasing the contrast of the phantom details (spherical cavity) immersed in the highly scattering layer (spherical cavity). However, large granularity is still observed in the images due to the presence of speckle noise. In the next experiment, the DM was switched off and image reconstructions were repeated for different illumination angles introduced by the galvo scanners [Fig. 4(3)]. Cross-sectional images were reconstructed by averaging 3D reconstructions registered for 10 different illumination angles. In this case the contrast of the image in the strongly scattering layer has slightly improved, but the presence of crosstalk does not allow the edge of the cavity to be distinguished—either in the cross-sectional images or in the LSF measured along the yellow dotted line [Figs. 4(c3) and 4(d3)]. Figure 4(4) shows the effect of applying both devices (a DM and galvo scanner). In this case, the improvement of the imaging contrast is visible due to the reduction of crosstalk as in Fig. 4(2), and there also is a reduction in the contrast of the speckle noise manifested by reduced graininess and finer reconstruction of imaged details [Figs. 4(a4) and 4(b4)]. Moreover, the corresponding LSFs are smoother, indicating improved localizations of the scattering phantom's details.

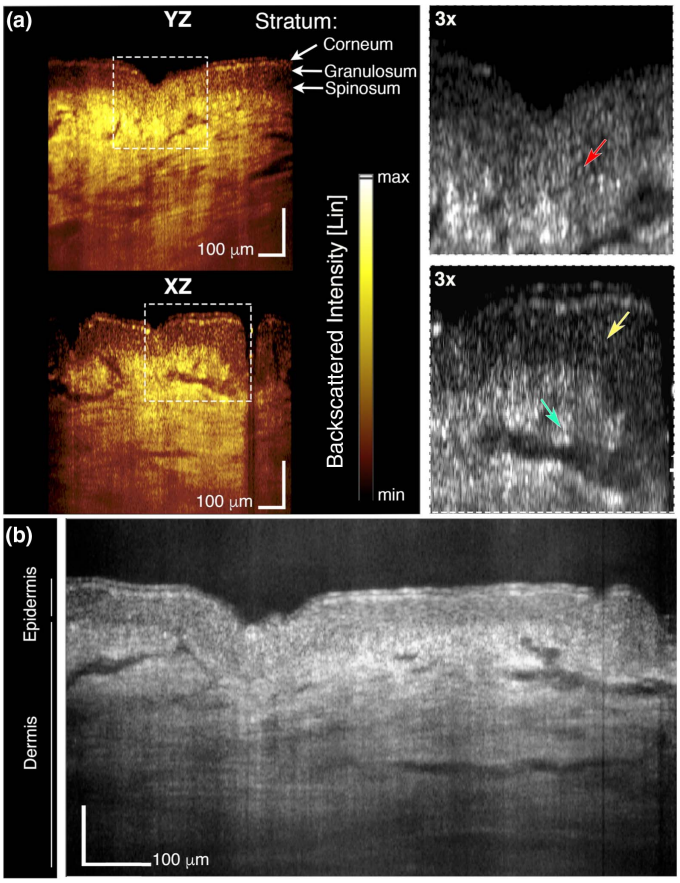

Fig. 6. Crosstalk-free FD-FF-OCT *in vivo* images of human forearm skin: (a) data visualized in linear scale for XZ and YZ cross-sections (optical B scans); red arrow indicates probable localization of individual melanocytes in the stratum spinosum; yellow arrow shows granular structure corresponding to cells in the stratum spinosum; green arrow indicates sebaceous glands in the dermis in proximity of a hair follicle; and (b) representative cross-sectional image displayed in logarithmic greyscale. Data used for full volumetric reconstruction (512 × 512 × 512 pixels) were acquired within 0.4 s (36 volumes).

We also compared the performance of our method to that of the scanning FD-OCT in terms of crosstalk suppression rather than sensitivity or overall performance of the systems. Nevertheless, we tried to keep similar parameters for both experiments. Both systems were equipped with the same ×10 objective (NA = 0.3).

The scanning OCT system uses a Ti:sapphire laser with the spectral bandwidth of 130 nm (FWHM) and a central wavelength of 800 nm. The measured axial resolution in the air was 2.5 μm. The exposition time of the 2048-pixel-line camera was 12.5 μs. We collected 512 × 512 A scans in 3.3 s when illuminating the sample with a beam of power of 2.5 mW. The energy per 3D pixel (voxel) delivered to the sample was $12.5 \cdot 10^{-6}$ s × $2.5 \cdot 10^{-3}$ W/2048 pixels = $15 \cdot 10^{-12}$ J/voxel.

In the case of FD-FF-OCT we acquired 36 volumes, each consisting of 1024 frames, 512 × 512 in size. Each frame was collected with an exposure time of 17 μs and the power on the sample was 6 mW. Due to the limited sweep range of the laser we could achieve axial resolution of 4.5 μm, but energy per 3D pixel was $36 \times (16.7 \cdot 10^{-6}$ s × $6 \cdot 10^{-3}$ W/$512^2) = 14 \cdot 10^{-12}$ J/voxel, which is similar to the energy delivered in the experiment with the scanning system. The FD-FF-OCT imaging of all averaged volumes was performed in 36 × 18.67 ms = 672 ms (16.67 ms + 2 ms for each volume, 2 ms added for changing the illumination angle), which is still five times faster than for the scanning OCT system.

Cross-sectional images measured by both techniques and corresponding LSFs of the scattering phantom are presented in Fig. 5. This comparison indicates that the crosstalk suppression in our new speckleless FD-FF-OCT device is comparable to the classical spectrometer-based, scanning FD-OCT instrument. To analyze the extent of signal-carrying speckle suppression we calculated speckle contrast defined as $K = \frac{\sigma_s^2}{\bar{I}_S}$, where $\bar{I}_S$ stands for averaged intensity over the area of signal, and σ_s is the standard deviation of signal intensity. The speckle contrast is reduced from 0.7 to 0.3 in XY projections and from 0.61 to 0.38 in XZ cross-section in favor of the proposed full-field technique. Slight differences in K values calculated for different projections most likely originate from inhomogeneous distribution of scattering centers and sparse localization of scattering clusters in the phantom.

6. *IN VIVO* IMAGING OF HUMAN SKIN

To test the performance of this new method, we carried out *in vivo* OCT imaging of human skin. To avoid strong specular reflections from the skin–air interface, a drop of glycerin was placed on the forearm and put in contact with a mechanically fixed 0.15 mm thick microscope cover glass. The glass plate was tilted with respect to the imaging plane of the objective lens. The glass-plate was mounted on an *xyz* translation stage to help with the sample alignment in the preview mode before the data

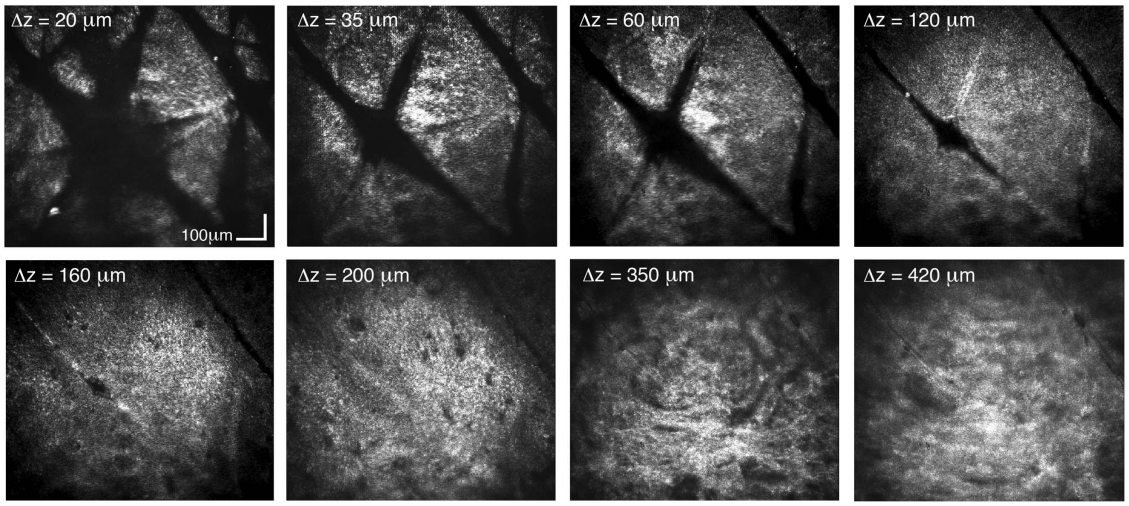

Fig. 7. Crosstalk-free FD-FF-OCT images of human forearm skin *in vivo*: XY cross-sections corresponding to various axial planes; Δz indicates the depth below the surface of skin.

acquisition. It is important to emphasize that the hand was not immobilized by any dedicated mechanical system to perform the imaging.

The preview mode provided real-time images while the arm was being adjusted to find a suitable imaging location. To reduce speckles and increase SNR we acquired 36 volumes with the angle of illumination changed between each volume by a pair of galvo scanners. The acquisition time of the full data set was 0.4 s. Figure 6 shows three representative cross-sectional images derived from the same 3D volumetric data set. Speckle reduction reveals anatomical details and enables greater differentiation of the tissue. It is possible to distinguish between the stratum corneum, the stratum granulosum, and the stratum spinosum layers—the three key components of human epidermis. The stratum spinosum layer is particularly well differentiated with a layer of polyhedral keratinocytes visible in crosstalk-free FD-FF-OCT as a granular layer.

Slightly higher axial and transverse resolution would probably reveal the regular structure of this layer [40,41]. In some locations, it is also possible to observe hyperreflective spots probably corresponding to melanocytes (red arrow in a zoomed-in image in Fig. 6). Identification of anatomical details in dermis would require further work—comparing OCT images with histology from the same location. We can speculate that some structures visible in cross-sectional images may correspond to sebaceous glands located in proximity of hair follicles (green arrow in a zoomed-in image in Fig. 6). Supplementary fly-through movies in scale expose rich structural details visible in both the epidermis and dermis (Visualization 1, Visualization 2, and Visualization 3).

Figure 7 presents representative *enface* images in the XY plane that are perpendicular to the direction of light propagation. The quality of images is comparable to that demonstrated with the state-of-the-art TD-FF-OCT [41]. However, in contrast to skin 3D images obtained by classic TD-FF-OCT, the imaging depth is five times larger.

7. DISCUSSION

We have demonstrated an efficient way to reduce crosstalk in a Fourier-domain, full-field optical coherence tomography system that uses a spatially coherent tunable laser source.

The crosstalk reduction was achieved by implementing random phase modulation. The phase modulation was carried out with a DM imprinted with time-varying and uncorrelated phase patterns across the beam wavefront at a half-a-megahertz rate. The dynamics of phase modulation imparted by the membrane at each spatial point was fast enough to significantly decrease the spatial coherence of the laser beam within 20 μs—the acquisition time of one image by the fast camera. The angular compounding was carried out by regular galvo scanners, which changed the angle of the illumination beam with respect to the sample between acquisitions of 3D volumes. Averaging of 36 of such 3D volumes resulted in a speckle reduction by a factor of 2 in the focal plane and increased SNR.

This study presents what we believe is the first realization of Fourier domain FF-OCT with a spatially incoherent swept laser source and the first demonstration of essentially crosstalk-free 3D volumes of scattering samples and skin acquired *in vivo* within less than a second.

In addition to being highly effective for crosstalk removal, it is a low-cost and robust add-on to any existing Fourier domain FF-OCT system, requiring only simple modifications.

To enable the widespread use of Fourier domain FF-OCT technology the price of the fast camera used here must be reduced, which could be expected with further development of CMOS technology. Moreover, improvement in other camera parameters, such as frame rate and full well capacity would further improve the system performance. A higher frame rate would mostly be beneficial for *in vivo* applications, whereas higher full well capacity would primarily help achieve deeper imaging depth. For example, a camera with 10 times overall photoelectron throughput already exists at a fraction of the price of the current camera and has been used in time domain FF-OCT [42]. The system would also benefit from improvements in swept laser parameters, such as power and spectral bandwidth. The latter would allow finer axial resolution and should be technically feasible with further laser development. The sweeping rate is not that critical in wide-field applications of OCT since the wavelength must change between frames, which is in contrast with the scanning Fourier domain OCT, where the change must happen between every scanning

point. Therefore, slower sweep rates, around 50 kHz, are adequate.

Another important parameter in Fourier-domain FF-OCT is the DOF defining the axial extent over which crisp images could be acquired. For highest lateral resolution microscopy systems, this value could be smaller than 1 μm, completely impeding 3D volume acquisition. A possible solution for short DOF is digital refocusing, which could partially reconstruct crisp images from acquired data via mathematical operations [43–46]. In time-domain FF-OCT this problem is solved by simply moving a sample physically along the axial direction. However, this also means that only one *en face* plane will be acquired compared to the 3D volume acquired in Fourier domain FF-OCT. Therefore, a slowdown in imaging speed by 2–3 orders of magnitude occurs.

Funding. Narodowe Centrum Nauki (NCN) (NCN, 2016/22/A/ST2/00313); European Union Horizon 2020 Framework Programme (H2020) (666295); Fundacja na rzecz Nauki Polskiej (FNP) (TEAM TECH/2016-3/20).

Acknowledgment. The authors acknowledge that the scientific work was funded from financial resources for science in the years 2016-2019, awarded for the implementation of an international co-financed project.

See Supplement 1 for supporting content.

REFERENCES

1. D. Huang, E. A. Swanson, C. P. Lin, J. S. Schuman, W. G. Stinson, W. Chang, M. R. Hee, T. Flotte, K. Gregory, C. A. Puliafito, and J. G. Fujimoto, "Optical coherence tomography," Science **254**, 1178–1181 (1991).
2. M. Wojtkowski, "High-speed optical coherence tomography: basics and applications," Appl. Opt. **49**, D30–61 (2010).
3. W. Drexler and J. G. Fujimoto, eds., *Optical Coherence Tomography* (Springer-Verlag, 2008).
4. A. F. Fercher, "Medical optics—Perspectives," Z. Med. Phys. **17**, 1–2 (2007).
5. J. M. Schmitt, "Optical coherence tomography (OCT): a review," IEEE J. Sel. Top. Quantum Electron. **5**, 1205–1215 (1999).
6. J. W. Goodman, "Some fundamental properties of speckle," J. Opt. Soc. Am. **66**, 1145–1150 (1976).
7. J. M. Schmitt, S. H. Xiang, and K. M. Yung, "Speckle in optical coherence tomography," J. Biomed. Opt. **4**, 95–105 (1999).
8. M. Bashkansky and J. Reintjes, "Statistics and reduction of speckle in optical coherence tomography," Opt. Lett. **25**, 545–547 (2000).
9. B. Karamata, K. Hassler, M. Laubscher, and T. Lasser, "Speckle statistics in optical coherence tomography," J. Opt. Soc. Am. A **22**, 593–596 (2005).
10. D. D. Duncan, S. J. Kirkpatrick, and R. K. K. Wang, "Statistics of local speckle contrast," J. Opt. Soc. Am. A **25**, 9–15 (2008).
11. D. Borycki, M. Nowakowski, and M. Wojtkowski, "Control of the optical field coherence by spatiotemporal light modulation," Opt. Lett. **38**, 4817–4820 (2013).
12. D. Borycki, M. Hamkało, M. Nowakowski, M. Szkulmowski, and M. Wojtkowski, "Spatiotemporal optical coherence (STOC) manipulation suppresses coherent cross-talk in full-field swept-source optical coherence tomography," Biomed. Opt. Express **10**, 2032–2054 (2019).
13. D. Hillmann, H. Spahr, C. Pfaffle, H. Sudkamp, G. Franke, and G. Huttmann, "In vivo optical imaging of physiological responses to photostimulation in human photoreceptors," Proc. Natl. Acad. Sci. USA **113**, 13138–13143 (2016).
14. D. Hillmann, H. Spahr, H. Sudkamp, C. Hain, L. Hinkel, G. Franke, and G. Huttmann, "Off-axis reference beam for full-field swept-source OCT and holoscopy," Opt. Express **25**, 27770–27784 (2017).
15. H. Spahr, C. Pfaffle, P. Koch, H. Sudkamp, G. Huttmann, and D. Hillmann, "Interferometric detection of 3D motion using computational subapertures in optical coherence tomography," Opt. Express **26**, 18803–18816 (2018).
16. B. Povazay, A. Unterhuber, B. Hermann, H. Sattmann, H. Arthaber, and W. Drexler, "Full-field time-encoded frequency-domain optical coherence tomography," Opt. Express **14**, 7661–7669 (2006).
17. B. Karamata, M. Laubscher, M. Leutenegger, S. Bourquin, T. Lasser, and P. Lambelet, "Multiple scattering in optical coherence tomography. I. Investigation and modeling," J. Opt. Soc. Am. A **22**, 1369–1379 (2005).
18. B. Karamata, M. Leutenegger, M. Laubscher, S. Bourquin, T. Lasser, and P. Lambelet, "Multiple scattering in optical coherence tomography. II. Experimental and theoretical investigation of cross talk in wide-field optical coherence tomography," J. Opt. Soc. Am. A **22**, 1380–1388 (2005).
19. D. J. Faber, F. J. van der Meer, and M. C. G. Aalders, "Quantitative measurement of attenuation coefficients of weakly scattering media using optical coherence tomography," Opt. Express **12**, 4353–4365 (2004).
20. A. Federici and A. Dubois, "Full-field optical coherence microscopy with optimized ultrahigh spatial resolution," Opt. Lett. **40**, 5347–5350 (2015).
21. J. Ogien and A. Dubois, "High-resolution full-field optical coherence microscopy using a broadband light-emitting diode," Opt. Express **24**, 9922–9931 (2016).
22. A. Dubois, L. Vabre, A.-C. Boccara, and E. Beaurepaire, "High-resolution full-field optical coherence tomography with a Linnik microscope," Appl. Opt. **41**, 805–812 (2002).
23. Y. Choi, P. Hosseini, W. Choi, R. R. Dasari, P. T. So, and Z. Yaqoob, "Dynamic speckle illumination wide-field reflection phase microscopy," Opt. Lett. **39**, 6062–6065 (2014).
24. R. Zhou, D. Jin, P. Hosseini, V. R. Singh, Y. H. Kim, C. Kuang, R. R. Dasari, Z. Yaqoob, and P. T. So, "Modeling the depth-sectioning effect in reflection-mode dynamic speckle-field interferometric microscopy," Opt. Express **25**, 130–143 (2017).
25. M. C. Pitter, C. W. See, and M. G. Somekh, "Full-field heterodyne interference microscope with spatially incoherent illumination," Opt. Lett. **29**, 1200–1202 (2004).
26. M. G. Somekh, C. W. See, and J. Goh, "Wide field amplitude and phase confocal microscope with speckle illumination," Opt. Commun. **174**, 75–80 (2000).
27. A. Safrani and I. Abdulhalim, "Ultrahigh-resolution full-field optical coherence tomography using spatial coherence gating and quasi-monochromatic illumination," Opt. Lett. **37**, 458–460 (2012).
28. B. Redding, Y. Bromberg, M. A. Choma, and H. Cao, "Full-field interferometric confocal microscopy using a VCSEL array," Opt. Lett. **39**, 4446–4449 (2014).
29. Y. Choi, T. D. Yang, K. J. Lee, and W. Choi, "Full-field and single-shot quantitative phase microscopy using dynamic speckle illumination," Opt. Lett. **36**, 2465–2467 (2011).
30. I. Sencan, B. K. Huang, Y. Bian, E. Mis, M. K. Khokha, H. Cao, and M. Choma, "Ultrahigh-speed, phase-sensitive full-field interferometric confocal microscopy for quantitative microscale physiology," Biomed. Opt. Express **7**, 4674–4684 (2016).
31. F. Shevlin, "Phase randomization for spatiotemporal averaging of unwanted interference effects arising from coherence," Appl. Opt. **57**, E6–E10 (2018).
32. W. Wang, H. Kozaki, J. Rosen, and M. Takeda, "Synthesis of longitudinal coherence functions by spatial modulation of an extended light source: A new interpretation and experimental verifications," Appl. Opt. **41**, 1962–1971 (2002).
33. B. Redding, M. A. Choma, and H. Cao, "Speckle-free laser imaging using random laser illumination," Nat. Photonics **6**, 355–359 (2012).
34. A. E. Desjardins, B. J. Vakoc, W. Y. Oh, S. M. Motaghiannezam, G. J. Tearney, and B. E. Bouma, "Angle-resolved optical coherence tomography with sequential angular selectivity for speckle reduction," Opt. Express **15**, 6200–6209 (2007).
35. A. E. Desjardins, B. J. Vakoc, G. J. Tearney, and B. E. Bouma, "Speckle reduction in OCT using massively-parallel detection and frequency-domain ranging," Opt. Express **14**, 4736–4745 (2006).
36. N. Iftimia, B. E. Bouma, and G. J. Tearney, "Speckle reduction in optical coherence tomography by "path length encoded" angular compounding," J. Biomed. Opt. **8**, 260–263 (2003).
37. H. Wang and A. M. Rollins, "Speckle reduction in optical coherence tomography using angular compounding by B-scan Doppler-shift encoding," J. Biomed. Opt. **14**, 030512 (2009).

38. C. Pfaffle, H. Spahr, D. Hillmann, H. Sudkamp, G. Franke, P. Koch, and G. Huttmann, "Reduction of frame rate in full-field swept-source optical coherence tomography by numerical motion correction [Invited]," Biomed. Opt. Express **8**, 1499–1511 (2017).
39. S. N. Lashansky, S. Mansbach, M. J. Berger, T. Karasik, and M. Bin-Nun, "Edge response revisited," Proc. SPIE **6941**, 69410Z (2008).
40. A. Dubois, O. Levecq, H. Azimani, D. Siret, A. Barut, M. Suppa, V. Del Marmol, J. Malvehy, E. Cinotti, P. Rubegni, and J. L. Perrot, "Line-field confocal optical coherence tomography for high-resolution noninvasive imaging of skin tumors," J. Biomed. Opt. **23**, 1–9 (2018).
41. J. Ogien and A. Dubois, "A compact high-speed full-field optical coherence microscope for high-resolution in vivo skin imaging," J. Biophoton. **12**, e201800208 (2019).
42. E. Auksorius and A. C. Boccara, "Fast subsurface fingerprint imaging with full-field optical coherence tomography system equipped with a silicon camera," J. Biomed. Opt. **22**, 1–8 (2017).
43. T. S. Ralston, D. L. Marks, P. S. Carney, and S. A. Boppart, "Interferometric synthetic aperture microscopy," Nat. Phys. **3**, 129–134 (2007).
44. N. D. Shemonski, F. A. South, Y. Z. Liu, S. G. Adie, P. S. Carney, and S. A. Boppart, "Computational high-resolution optical imaging of the living human retina," Nat. Photonics **9**, 440–443 (2015).
45. A. Kumar, W. Drexler, and R. A. Leitgeb, "Numerical focusing methods for full field OCT: a comparison based on a common signal model," Opt. Express **22**, 16061–16078 (2014).
46. A. Kumar, L. M. Wurster, M. Salas, L. Ginner, W. Drexler, and R. A. Leitgeb, "In-vivo digital wavefront sensing using swept source OCT," Biomed. Opt. Express **8**, 3369–3382 (2017).